PHOTONICS Research

Towards low-frequency acoustic sensing using antiresonant hollow-core fibers

Meng Ding,[1] William Luocheng Wu,[2,*] Thomas W. Kelly,[1] Gregory T. Jasion,[1] Ian A. Davidson,[1] Ali Masoudi,[1] Paul White,[2] Francesco Poletti,[1] and Radan Slavík[1]

[1]Optoelectronics Research Centre, University of Southampton, Southampton SO17 1BJ, UK
[2]Institute of Sound and Vibration Research, University of Southampton, Southampton SO17 1BJ, UK
*Corresponding author: william.wu@soton.ac.uk

Received 11 November 2025; revised 21 January 2026; accepted 24 January 2026; posted 27 January 2026 (Doc. ID 584448); published 24 April 2026

Low-frequency acoustic waves exhibit low attenuation and strong penetration, enabling propagation over long distances in water and the solid Earth. This capability underpins applications in natural-hazard monitoring and early warning (earthquakes, tsunamis, volcanic activity), long-range marine sensing and surveillance, and structural and equipment-health monitoring in harsh environments. Traditional piezoelectric hydrophones suffer from high self-noise and electro-magnetic interference, motivating the exploration of fiber optic solutions. However, the operation of fiber solutions at low frequencies suffers from temperature cross-sensitivity due to the inherent thermal sensitivity of conventional optical fibers. Hollow-core fibers (HCFs), which guide light in air/vacuum, provide lower thermal and higher acoustic sensitivity than conventional solid core fibers; however, the extent to which they could address this limitation has never been studied. Here, we present a comprehensive study of the acoustic and thermal sensitivities of HCFs, combining theoretical modeling and experimental validation, aiming for high acoustic sensitivity while keeping thermal sensitivity low, hence reducing unwanted cross-sensitivity. We validate its results experimentally on three HCFs with different structural compositions, quantifying the trade-off between acoustic and temperature sensitivities. Besides, we demonstrate a substantial improvement in temperature–acoustic decoupling by employing an HCF made from Ti-doped ultralow-expansion (ULE) glass, achieving a reduction in thermal sensitivity by more than three orders of magnitude compared with standard single-mode fiber while maintaining comparable acoustic sensitivity. Further, based on the theoretical model we have developed, we show that more optimal coating material could improve the performance of ULE-HCF by another two orders of magnitude. This work thus guides comprehensive design of thermally stable and acoustically sensitive HCF sensors for low-frequency acoustic sensing.

https://doi.org/10.1364/PRJ.584448

1. INTRODUCTION

By detecting the optical phase changes induced by acoustic pressure, optical fibers have found widespread application as acoustic sensors in diverse fields. Recently, increasing attention has been given to the detection of low-frequency acoustic signals, which propagate over long distances owing to their low attenuation and subsequent strong penetration capability. This capability is particularly valuable for applications including natural disaster monitoring and early warning (e.g., earthquakes [1], tsunamis [2], and volcanic activity [3]), infrastructure surveillance (such as railways and tunnels [4]), and marine sensing.

A key challenge in optical fiber acoustic sensors operating in the low-frequency range is temperature-induced phase drift, which introduces phase changes that may overlap in frequency with the acoustic waves of interest [5–11]. For example, distributed acoustic sensing (DAS) measurements can be affected by low-frequency noise possibly associated with the effect of temperature [5,10,11], leading to severe degradation in accuracy. Besides Earth monitoring mentioned earlier, this limitation is also acute in environments with high or rapidly varying temperatures (e.g., engine rooms, nacelles, exhaust trunks, or cryogenic transitions), where temperature cross-sensitivity can mask true acoustic/vibration signals.

Various approaches have been explored to mitigate temperature cross-sensitivity, including the use of fiber Bragg gratings (FBGs) and Fabry–Perot interferometers (FPIs) in differential or reference-based configurations to decouple acoustic and

temperature-induced responses [12]. While effective in certain scenarios, such approaches typically rely on additional compensation schemes and are often implemented as point sensors, which can increase system complexity and limit scalability. Therefore, other attempts have been made to mitigate the temperature cross-sensitivity of sensors themselves [6,13,14].

Hollow-core fibers (HCFs) offer a promising solution to overcome these limitations by guiding light predominantly in an air- or vacuum-filled core, which significantly reduces the interaction between the guided mode and the surrounding glass. As a result, HCFs exhibit both strongly reduced temperature sensitivity—since temperature-induced refractive index changes in glass are largely eliminated [15]—and enhanced acoustic sensitivity, owing to their increased mechanical compliance and the absence of pressure-induced refractive index effects that partially cancel the strain response in SMFs [16].

Previous studies on HCF acoustic sensors have mainly focused on photonic bandgap HCFs [17–19], while the current low-loss HCFs (e.g., with losses below 0.1 dB/km [20,21]) are based on antiresonant guidance, such as (double) nested antiresonant nodeless fiber [(D)NANF] geometries [22]. Antiresonant HCFs such as DNANF remain underexplored in the context of acoustic sensing. Given their ultralow loss and unique mechanical properties, antiresonant fibers hold great promise for low-frequency acoustic detection.

This paper systematically explores the acoustic sensitivities of HCFs and their cross-sensitivity to temperature. Our study particularly focuses on examining the effects of bare fiber diameter, air hole size, coating thickness, and material properties on both acoustic and thermal responsiveness. By combining simulations with experimental verification, this research provides insights into how these structural parameters can be optimized to enhance sensor performance, enabling the development of next-generation optical fiber acoustic sensors.

2. THEORETICAL ANALYSIS

A. Response to Pressure

The phase accumulated by light with wavelength λ, propagating in a fiber of length L and effective refractive index n_{eff}, is

$$\varphi = \frac{2\pi n_{\text{eff}} L}{\lambda}. \tag{1}$$

An acoustic pressure applied to the fiber causes changes in both n_{eff} and L, which consequently affect the accumulated phase φ. The rate of this change is characterized by the fiber normalized acoustic pressure sensitivity of

$$S_p = \frac{1}{\varphi}\frac{\mathrm{d}\varphi}{\mathrm{d}p} = \frac{1}{n_{\text{eff}}}\frac{\mathrm{d}n_{\text{eff}}}{\mathrm{d}p} + \frac{1}{L}\frac{\mathrm{d}L}{\mathrm{d}p}, \tag{2}$$

where the right-hand side is obtained using Eq. (1).

In antiresonant HCFs [e.g., with NANF structure shown in Fig. 1(a)], most of the light propagating in the fiber (typically >99.99%) is guided in the hollow-core region. As the refractive index of the gas inside the HCF's core remains constant for an HCF with sealed ends (no gas entering or leaving) [23], the n_{eff} variations due to acoustic pressure are negligible. The first term on the right-hand side of Eq. (2) can thus be neglected in HCFs, meaning their acoustic response is driven mainly by the axial strain response to external pressure:

$$S_p \approx \frac{1}{L}\frac{\mathrm{d}L}{\mathrm{d}p}. \tag{3}$$

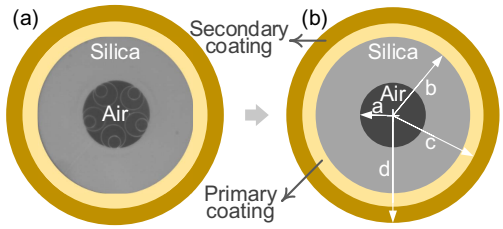

Fig. 1. Example of a cross-section of NANF type antiresonant HCF (a) and its simplified model used in our acoustic sensitivity analysis, which neglects the internal structure (b).

In SMFs, the first term on the right-hand side of Eq. (2), has opposite sign to the second term (fiber elongation due to acoustic pressure causes a reduction in n_{eff}). This makes SMF's acoustic sensitivity smaller than that of HCFs, where no such partial cancellation of the two terms occurs.

To analyze the acoustic response of HCFs, we neglect the contribution of the microstructure surrounding the core, as it contains minimum amount of glass material. This enables us to model the fiber as a silica capillary, Fig. 1(b), with inner radius a and outer radius b. We also consider it to be coated with up to two coating layers with outer radii of c and d [Fig. 1(b)], representing a common fabrication scenario.

Each layer characterized by Young's modulus E and Poisson ratio ν, is assumed to be homogeneous, isotropic, and perfectly bonded to the adjacent layers. The fiber is assumed to be subjected to a uniform external acoustic pressure P at the outer boundary $r = d$, while the inner air–glass interface at $r = a$ is assumed to be stress-free.

The assumption of a uniform acoustic field is justified by the geometric scale of the here-studied fiber, surrounding environment considered (water), and the low-frequency acoustic range considered in this work. Specifically, the maximum considered excitation frequency is 1 kHz, and with the speed of sound in water being ~1500 m/s, the corresponding acoustic wavelength is >1.5 m. This is more than an order of magnitude larger than the studied fiber coil diameter (10 cm) and many orders of magnitude larger than the fiber diameter itself. Consequently, the acoustic pressure acting on the entire fiber coil can be regarded as spatially uniform. For the same reason, frequency-dependent effects, including directional sensitivity and structural acoustic resonances of the fiber, are neglected [24].

Under axisymmetric loading, the mechanical deformation is governed by classical elasticity theory in cylindrical coordinates. The stress of each layer is given by

$$\sigma_r^{(i)} = B_i + \frac{C_i}{r^2}, \quad \sigma_\theta^{(i)} = B_i - \frac{C_i}{r^2}, \quad \sigma_z^{(i)} = D_i. \tag{4}$$

Here, B_i, C_i, and D_i are the coefficients to be determined by boundary conditions. The corresponding strains in each layer are given by

$$\varepsilon_r^{(i)} = \frac{1}{E_i}[\sigma_r^{(i)} - \nu_i(\sigma_\theta^{(i)} + \sigma_z^{(i)})],$$
$$\varepsilon_\theta^{(i)} = \frac{1}{E_i}[\sigma_\theta^{(i)} - \nu_i(\sigma_r^{(i)} + \sigma_z^{(i)})],$$
$$\varepsilon_z^{(i)} = \frac{1}{E_i}[\sigma_z^{(i)} - \nu_i(\sigma_r^{(i)} + \sigma_\theta^{(i)})]. \quad (5)$$

Applying plane-strain approximation and hydrostatic conditions, the boundary and continuity conditions can be summarized as follows[17].

Inner boundary: $\sigma_r^{(2)}(a) = 0$,

Outer boundary: $\sigma_r^{(4)}(d) = -P$,

Continuity of stress: $\sigma_r^{(2)}(b) = \sigma_r^{(3)}(b),\ \sigma_r^{(3)}(c) = \sigma_r^{(4)}(c)$,

Continuity of displacement: $u_r^{(2)}(b) = u_r^{(3)}(b),\ u_r^{(3)}(c) = u_r^{(4)}(c)$,

Axial strain uniformnity: $\varepsilon_z^{(2)} = \varepsilon_z^{(3)} = \varepsilon_z^{(4)} = \varepsilon_z$,

Hydrostatical condition: $(b^2 - a^2)\sigma_z^{(2)} + (c^2 - b^2)\sigma_z^{(3)}$
$+ (d^2 - c^2)\sigma_z^{(4)} = -P \cdot d^2$, (6)

where $u(r)$ is the displacement. In an axisymmetric cylindrical structure, it can be expressed as

$$u(r) = r \cdot \varepsilon_\theta(r). \quad (7)$$

By combining all these equations, the axial strain ε_z can be obtained, and the acoustic sensitivity can be calculated as [25]

$$S_p = \frac{\varepsilon_z}{P}. \quad (8)$$

In practice, acoustic sensitivity is usually expressed with a unit of dB re μPa^{-1}. The conversion is performed as $S_p^{dB} = 20\log_{10}(S_p) - 120$ when the pressure unit in Eq. (8) is Pa.

B. Response to Temperature

Variations in ambient temperature also cause changes in the accumulated phase φ [given by Eq. (1)]. This is characterized by the fiber thermal sensitivity:

$$S_T = \frac{1}{\varphi}\frac{d\varphi}{dT} = \frac{1}{n_{eff}}\frac{dn_{eff}}{dT} + \frac{1}{L}\frac{dL}{dT}. \quad (9)$$

The right-hand side of Eq. (9) was obtained using Eq. (1). Similar to pressure sensitivity [Eq. (3)], the temperature-induced refractive index change can be neglected in sealed HCFs [23], making temperature-induced HCF length changes the dominant contributor to their thermal sensitivity. Using the simplified HCF structure shown in Fig. 1(b), this term can be calculated as [26]

$$S_T \approx \frac{1}{L}\frac{dL}{dT} = \frac{\sum_i \alpha_i E_i A_i}{\sum_i E_i A_i}. \quad (10)$$

Here, α_i and A_i are the coefficient of thermal expansion (CTE) and cross-sectional areas of silica glass ($i = 1$), inner coating ($i = 2$), and outer coating ($i = 3$).

C. Simulations

To explore the design dependencies of the acoustic and thermal responses in HCFs, we conducted a series of simulations by varying key structural and mechanical parameters of the fiber geometry and coating material. Our aim was to provide clear design guidelines for developing HCFs that offer high acoustic sensitivity while minimizing temperature crosstalk.

In the initial analysis, we used a simplified HCF design structure that considers a single coating layer made of acrylate, which is the most commonly used optical fiber coating material [18]. Its properties strongly depend on the fabrication recipe [27]. Here, we use parameters shown in Table 1, which were reported to be used on a single-coated HCF. The table also shows the properties of silica and ultra-low expansion (ULE) glasses, which are the glass materials used in the experimental work reported here.

To evaluate the effect of each parameter independently, we varied one of the HCF structure parameters at a time while keeping the rest constant, at a value that is typically used in fabricated HCFs or at a value at which the parameter studied changes the performance very weakly.

To evaluate the best performance in our target application, which aims at maximizing the acoustic sensitivity while keeping the thermal sensitivity as low as possible, we introduce a figure of merit (FoM) that we normalize to the performance of SMF as

$$F_m = \frac{S_p^{HCF}}{S_p^{SMF}} \cdot \frac{S_T^{SMF}}{S_T^{HCF}}, \quad (11)$$

where S_p^{SMF} and S_T^{SMF} are acoustic and thermal sensitivities of the SMFs, respectively. When calculating FoM, we take the linear value of acoustic sensitivity with a unit of Pa^{-1}. For S_p^{SMF}, we use the value of 1.26×10^{-11} Pa^{-1} (−338 dB re μPa^{-1}), which we calculated using the above-mentioned approach. In the experiments that follow, we confirm the validity of this value. As for the thermal sensitivity, we use $S_T^{SMF} = 11$ ppm/°C (ppm, parts per million), which is a value reported in Ref. [29].

We first investigate the effect of cladding radius [parameter b shown in Fig. 1(b)] by varying it between 40 and 140 μm while fixing both the air hole radius [parameter a in Fig. 1(b)] and coating thickness at 30 μm. As shown in Fig. 2(a), both acoustic sensitivity and thermal sensitivity decrease with increasing cladding diameter. Within the selected range of cladding diameters, the acoustic sensitivity decreases by 12 dB, from −326 to −338 dB re μPa^{-1}, while the thermal sensitivity reduces by a factor of 3.7 (corresponding to 5.7 dB), from 1.7 to 0.45 ppm/°C. Besides, to examine our simplification of our model, we performed numerical simulations on NANF structures that include the antiresonant cladding geometry here.

Table 1. Material Properties of Cladding and Coating Used in Simulations

Material	Young's Modulus	Poisson's Ratio	CTE (ppm/°C)
Silica	72 GPa	0.17	0.3 [28]
Acrylate	200 MPa [26]	0.37 [18]	110 [26]
ULE	67.6 GPa	0.17	−0.04 [29]

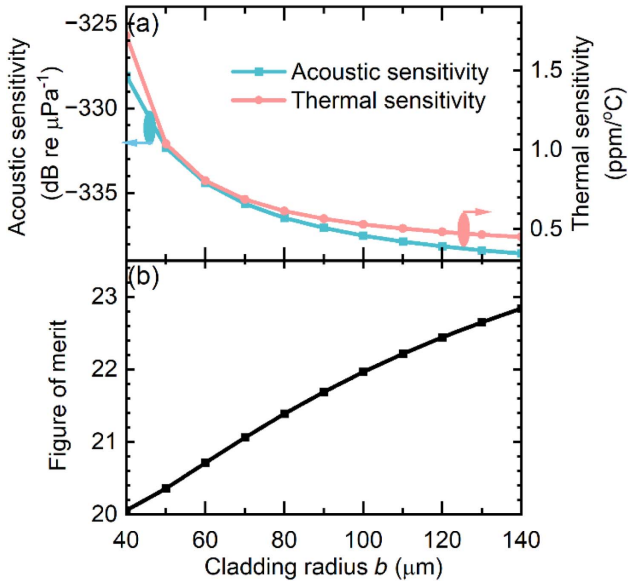

Fig. 2. Numerical analysis of the acoustic and thermal sensitivities of HCFs as a function of the cladding diameter (a), and corresponding FoM (b).

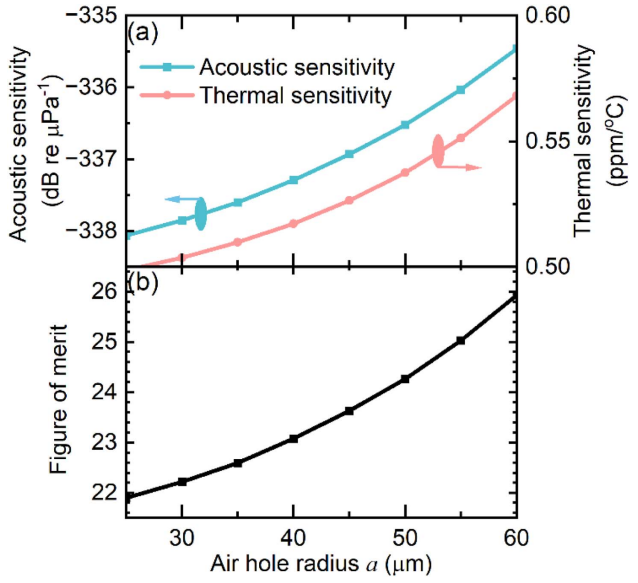

Fig. 3. Numerical analysis of the acoustic and thermal sensitivities of HCFs as a function of the air hole radius a (a), and corresponding FoM (b).

The calculated difference in acoustic sensitivity between the full microstructure model and the simplified homogeneous capillary model was found to be very small, <0.2 dB. Furthermore, this difference decreases with increasing outer cladding glass content, falling below 0.1 dB for cladding radii larger than 90 μm, confirming that the simplified model provides an accurate approximation for the fibers studied in this work.

The FoM calculated from data in Fig. 2(a) is shown in Fig. 2(b). Here, we see that it improves with the increasing cladding radius b, although this change is relatively modest, especially for $b > 70$ μm. In the following analysis, we fix the cladding radius to 110 μm.

The next parameter studied is the radius of the air hole a, which affects the fiber's mechanical properties, Fig. 3. By varying it from 25 to 60 μm, we cover the typical range found in most antiresonant fibers [21,22,30–32]. Over this range, we observed relatively modest changes in both acoustic and thermal sensitivities: less than 3 dB variation in acoustic sensitivity and below 0.1 ppm/°C in thermal sensitivity. However, the FoM improves with the increasing hole radius a. This is because the cladding glass mass decreases with increased hole radius a. In the following analysis, we use $a = 45$ μm as this is the size of the latest low-loss HCF [21].

To examine the role of the coating thickness, we varied it from 10 μm (as thin as demonstrated in Ref. [28]) to 100 μm. As shown in Fig. 4(a), both acoustic and thermal sensitivities increased with coating thickness. Thicker coatings provide more mechanical compliance, enhancing acoustic strain transfer. However, this improvement in acoustic response is accompanied by a substantial increase in thermal sensitivity due to a high thermal expansion coefficient of the coating. As a result, the FoM decreases from 29 to 16 across the considered coating thickness range, Fig. 4(b). For subsequent studies, we choose a 30 μm coating thickness, as thicker coatings lead to reduction in the FoM, while thinner coatings are more challenging to fabricate and use.

Many of the trade-offs discussed above are strongly influenced by the fiber coating. Thus, we also studied the influence of the coating Young's modulus. Acrylate coating can be prepared with a large range of Young's moduli, and harder/softer coatings have been reported in the literature. Thus, we consider a wide range of Young's modulus, spanning over five orders of magnitude, from 1 MPa to 100 GPa, Fig. 5. Here we see the acoustic sensitivity remains nearly constant in the low-modulus range (1–100 MPa) but begins to deteriorate significantly beyond 1 GPa [Fig. 5(a)]. This behavior is attributed to the increased stiffness of the coating, making the whole fiber hard to compress. In contrast, the thermal sensitivity remains relatively low and stable when the Young's modulus is below ∼1 GPa, but increases sharply with stiffer coatings due to higher thermal stress between the glass and coating. The resulting FoM, Fig. 5(b), drops from ∼41 at 1 MPa to below 2 at above 5 GPa of Young's modulus. These results suggest that employing low-Young's-modulus (below 10 MPa) coating minimizes the acoustic-temperature cross-sensitivity performance of the HCFs.

Besides Young's modulus, Poisson's ratio can also be varied via the choice of coating. We consider values between 0.1 and 0.5, while keeping the coating thickness of 30 μm and Young's modulus of 200 MPa, Fig. 6(a). We see that the acoustic sensitivity reduces with increasing Poisson's ratio. This is because higher Poisson's ratios result in larger lateral expansion under axial compression, thereby weakening the radial deformation needed to enhance acoustic response. In contrast, the thermal sensitivity remains nearly constant across the entire range, as Poisson's ratio has a limited influence on thermally induced expansion. As a result, FoM, Fig. 6(b), exhibits a substantial decline from ∼31 to ∼18 as Poisson's ratio increases from 0.1 to

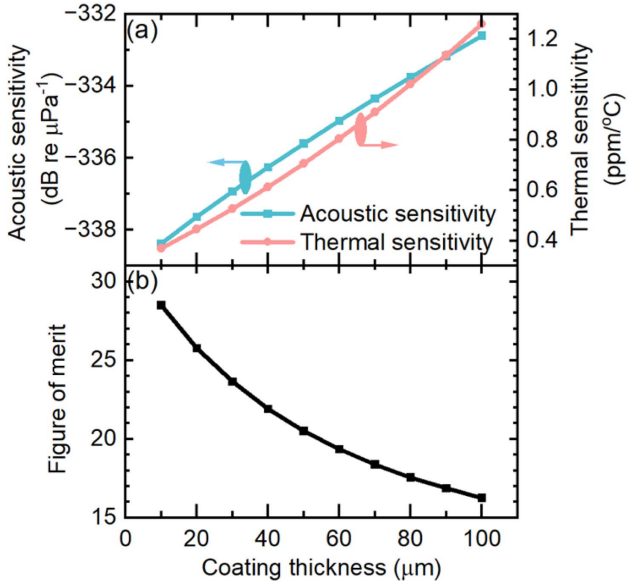

Fig. 4. Numerical analysis of the acoustic and thermal sensitivities of HCFs as a function of the coating thickness (a), and corresponding FoM (b).

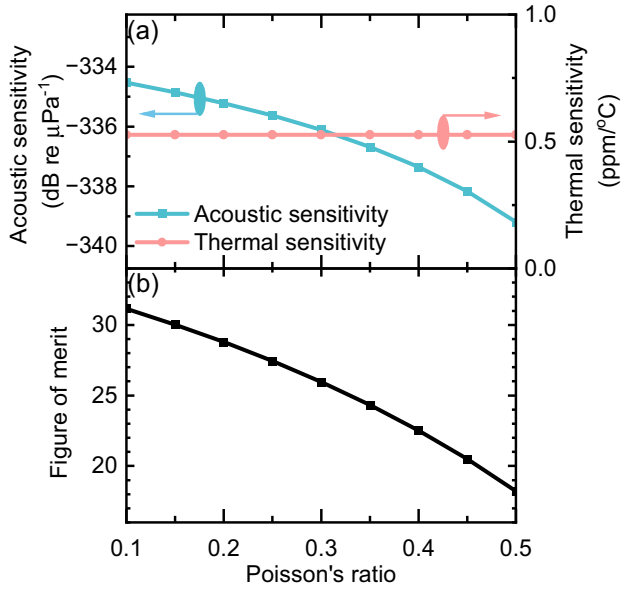

Fig. 6. Numerical analysis of the acoustic and thermal sensitivities of HCFs as a function of coating Poisson's ratio (a), and corresponding FoM (b).

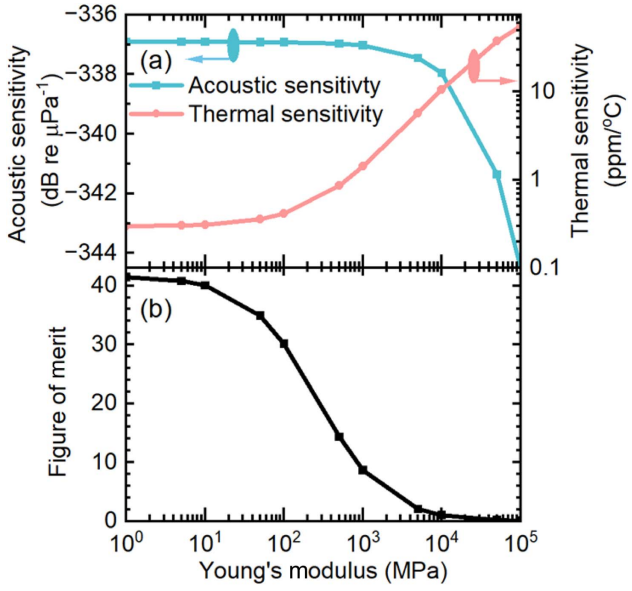

Fig. 5. Numerical analysis of the acoustic and thermal sensitivities of HCFs as a function of the coating Young's modulus (a), and corresponding FoM (b).

0.5. These results indicate that coating materials with lower Poisson's ratios are favorable for reducing the acoustic-temperature cross-sensitivity of HCFs.

From our analysis, it follows that silica-made HCFs will typically have FoMs in the range of 20–30, which could be further improved to about 50 with the right choice of coating material and thickness. The factor of 20–50 represents an important improvement over SMF, suggesting HCFs will significantly improve low-frequency acoustic sensor performance.

However, if further improvements are needed, HCFs from different materials would be required. We recently reported on HCFs made of ULE glass, which strongly reduces thermal sensitivity [29]. Together with the reduction in Young's modulus of ULE as compared to silica, this should lead to a significantly improved FoM. This is demonstrated in Fig. 7 where we show calculated acoustic sensitivity and thermal sensitivity of HCFs made of ULE glass with an air hole radius $a = 45$ μm and a cladding radius $b = 110$ μm with different coating thicknesses.

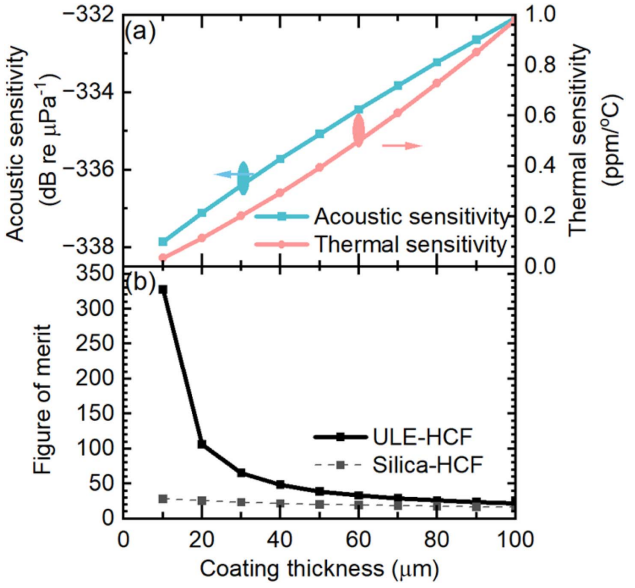

Fig. 7. Numerical analysis of the acoustic and thermal sensitivities of HCFs made of ULE glass as a function of coating thickness (a), and corresponding FoM (b). As a comparison, we also put silica-HCF FoM in (b). Solid line: ULE-HCF; dashed line: silica-HCF.

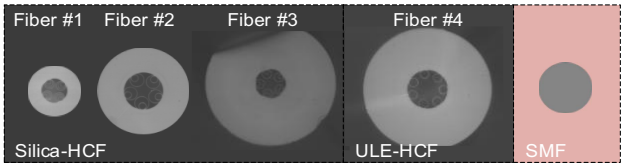

Fig. 8. Cross-sectional images of stripped (no coating) HCFs that we tested. The scale of all HCFs is the same, and we also put an image of SMF with a diameter of 125 μm to enable direct comparison of their sizes.

As we see, the ULE-glass HCF achieves an FoM more than 10 times larger than that of silica-glass HCFs at 10 μm coating thickness, which represents over 300 times improvement over SMFs. The simulation also suggests that ULE-HCF's FoM is significantly influenced by coating thickness, as its thermal sensitivity mainly comes from the coating.

3. HCF SAMPLES

The equations outlined in the previous section suggest that both thermal and pressure sensitivities depend on the mechanical properties of the used materials (fiber, coating) as well as on their dimensions. Thus, out of HCF samples available to us, we chose four samples that represent the largest variation in these characteristics. The selected HCFs are shown in Fig. 8.

The first three HCFs (Fibers #1–#3) were fabricated from pure silica glass, with DNANF (Fiber #1) and NANF (Fibers #2, #3) geometries. Fiber #4 was drawn from ULE glass using standard stack-and-draw techniques similar to those employed for silica-based HCFs and has a simple tubular geometry [29]. In the future, DNANF and NANF structures can be also made to achieve a lower transmission loss, as discussed in Ref. [29]. Fibers #3 and #4 both have a coating thickness of 30 μm, which represents a compromise between low thermal sensitivity and mechanical robustness [28,33]. The microstructure geometry should play a negligible role in the pressure and temperature responses, as discussed in the theoretical analysis part and associated simplification shown in Fig. 1(b). The difference between the samples can be appreciated from Fig. 8 with the same scale for all samples, and from Table 2 that summarizes their key parameters. Only Fiber #1 is dual coated, while the rest have a single coating.

4. EXPERIMENTS

A. Measurement Setup

The experimental setup used to measure the acoustic sensitivity of fibers under test (FUTs) is shown in Fig. 9. Each FUT was coiled with a diameter of 10 cm and hung horizontally in the center of a water tank with a diameter of 60 cm [34]. A reference hydrophone (Brüel & Kjær 8105) was placed at the center of the FUT coil to monitor the acoustic pressure at the same water level as the FUT.

Table 2. Size, Characterized by Parameters *a*, *b*, *c*, *d*, Defined in Fig. 1(a) of the Tested HCFs

	Cladding Material	*a* (μm)	*b* (μm)	*c* (μm)	*d* (μm)
Fiber #1	Silica	30	62.5	92.5	122.5
Fiber #2		46	108	168	
Fiber #3		35	147.5	177.5	
Fiber #4	ULE glass	45	145	175	

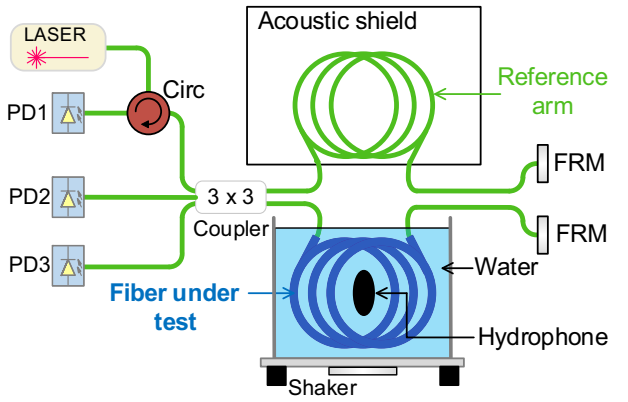

Fig. 9. Experimental setup for acoustic sensitivity characterization. FRM: Faraday rotator mirror; PD: photodiode; Circ: circulator.

The phase changes φ were extracted using an SMF-based Michelson interferometer, Fig. 9. In the sensing arm, the FUTs were fusion-spliced to standard SMFs with a segment of graded-index (GRIN) fiber being used as a mode-field adapter [35]. For the ULE-HCF, although ULE glass has a melting temperature ~100°C lower than silica [29], it was fusion-spliced using the same approach with appropriately adjusted parameters, thereby demonstrating compatibility with standard SMF-based systems. In the reference arm, SMF has the same optical length as the sensing arm. This optical path balance minimizes the changes of interference pattern due to laser wavelength drift during the measurement, while the use of Faraday rotator mirrors (FRMs) ensures polarization insensitivity of the interference contrast.

For unambiguous phase demodulation, a 3×3 coupler method was used [28]. The interferometer was illuminated by a narrow-linewidth fiber laser (central wavelength: 1556 nm; linewidth: <10 kHz).

Acoustic excitation was provided by a shaker mounted beneath the water tank. A sinusoidal electrical signal drove the shaker, generating a single-frequency acoustic field in the water. The resulting phase changes in the fiber were detected by the interferometer, while the acoustic pressure was simultaneously measured by the hydrophone. An example of measurement of the 100 Hz acoustic signal with a duration of 100 ms is shown in Fig. 10. In the real case, we measured the signals for 5 s, and then both signals were subjected to fast Fourier transform (FFT) analysis, enabling the extraction of the sound pressure amplitude ΔP and the corresponding phase change $\Delta\varphi$ in the tested HCF. The measured acoustic sensitivity was then calculated as defined in Eq. (1):

$$S_p = \frac{1}{\varphi}\frac{\mathrm{d}\varphi}{\mathrm{d}p} = \frac{\lambda}{2\pi L}\frac{\Delta\varphi}{\Delta P}. \tag{12}$$

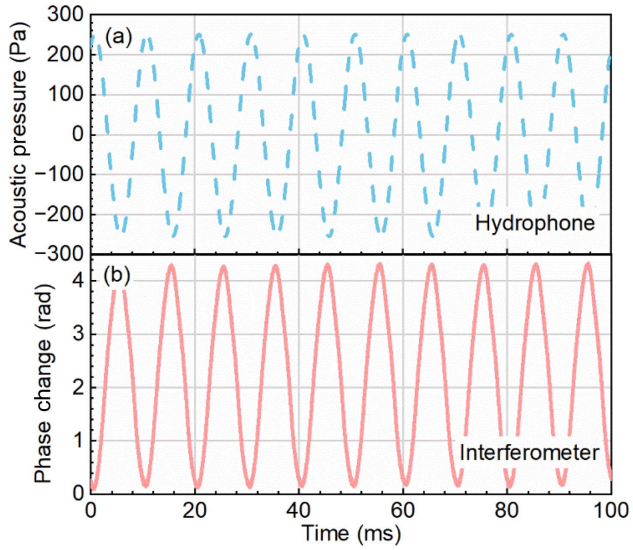

Fig. 10. An example of the hydrophone extracted acoustic pressure when the shaker was set to frequency of 100 Hz (a) and extracted phase change from the interferometer (b).

We scanned the excited acoustic wave frequency from 100 to 1000 Hz in steps of 100 Hz.

B. Experimental Results

The measured acoustic sensitivity was evaluated using the phase φ extracted from the interferometer used in Eq. (12). The results are shown in Fig. 11(a). Unexpectedly, significant fluctuations exceeding 15 dB were observed within the measured frequency range. We presume this was mainly due to the limited diameter (60 cm) of the water tank, which may cause non-uniform acoustic pressure distribution patterns at different frequencies due to reflection at boundaries (e.g., water and tank), especially for those acoustic signals above 500 Hz. This would cause different readings of the reference hydrophone that operates as a point detector, while the fiber coil operates as a ring-shaped detector. To address this, we used a coil of single-mode fiber (SMF28e, Corning Inc.) as a reference. It had the same diameter as the FUT coil. Subsequently, we evaluated the relative acoustic sensitivity of the tested HCFs against this SMF reference, as shown in Fig. 11(b). The revised measurements show smaller variation over measured frequencies (<10 dB) than shown in Fig. 11(a), supporting our hypothesis that the measurement is strongly influenced by the accuracy of the reference acoustic pressure measurement. In realistic field deployments, such as underwater or buried fiber installations, boundary-induced pressure non-uniformities are expected to be substantially reduced, particularly at low frequencies. Consequently, the uniform-pressure approximation employed in the theoretical analysis is generally more applicable in practical sensing environments than in the laboratory-scale setup used here. Importantly, these results show clear differences in relative acoustic sensitivity of the four FUTs compared to the SMF. To further validate the reliability of our measurement, we conducted simulations using the approach presented in Section 2, with results shown in Fig. 11(b). The simulated relative acoustic sensitivities with respect to the SMF show good agreement with the experimental results, with Fibers #3 and #4 having similar acoustic sensitivities to SMF28e, while Fibers #1 and #2 have significantly higher acoustic sensitivity than SMF28e. This higher acoustic sensitivity is attributed to their thick coating and lower stiffness due to their large air hole radii a.

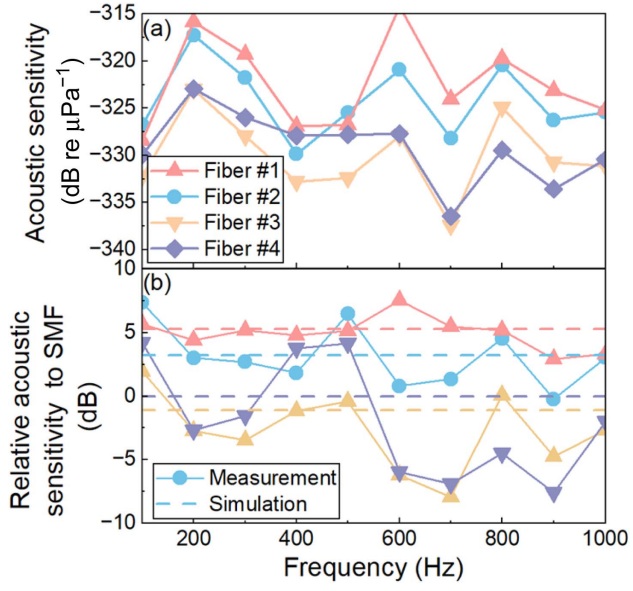

Fig. 11. Measured acoustic sensitivity of the tested HCFs when referenced with the hydrophone (a) and SMF-28e coil (b). Scatters: measured; dashed lines: simulated.

5. DISCUSSION

A. Acoustic/Thermal Characteristics of HCF Samples Studied

We summarize the acoustic and thermal sensitivities and associated FoMs of the four tested HCFs and compare them to those of SMF28e in Fig. 12. The acoustic sensitivities were taken as the average values of measurements in Fig. 11. The thermal sensitivities were taken from our previous measurements [26,29,36]. Due to large differences in thermal sensitivities, the x-axis is shown on a log scale.

We can see that the acoustic sensitivity of measured silica-made HCFs varies by about a factor of three (between 0.8 and 2.2 relative to SMF28e); however, the FoM shows a smaller variation of 14 to 28. This FoM range, which is in line with our expectations from our theoretical analysis, is due to higher acoustic sensitivity being accompanied by higher thermal sensitivity. For example, Fiber #1 exhibits an acoustic sensitivity 2.4 times that of Fiber #3 while its thermal sensitivity is 4.5 times higher. Nevertheless, the experiments confirm that silica-made HCFs can achieve FoM 20 times higher than SMF28e, making HCFs significantly more suitable for low-frequency acoustic sensing.

A promising strategy to decouple acoustic and thermal sensitivities is to use ULE-glass-made HCFs (Fiber #4). As shown in Fig. 12, Fiber #4 demonstrates a thermal sensitivity >1000 times lower than that of SMF28e while having an increased

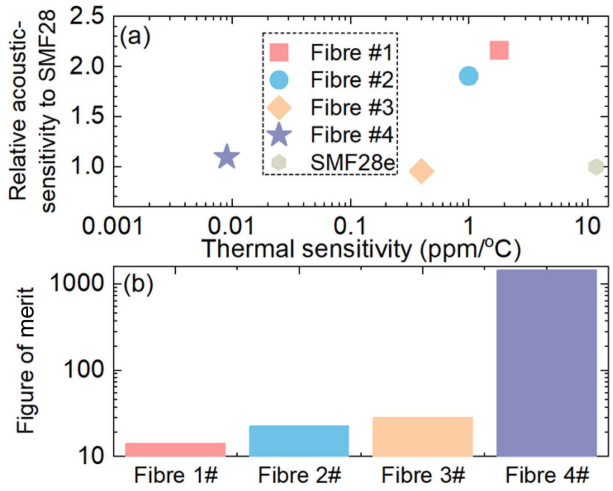

Fig. 12. Comparison of relative acoustic and thermal sensitivities of measured HCFs with respect to SMF28e (a) and their FoM (b).

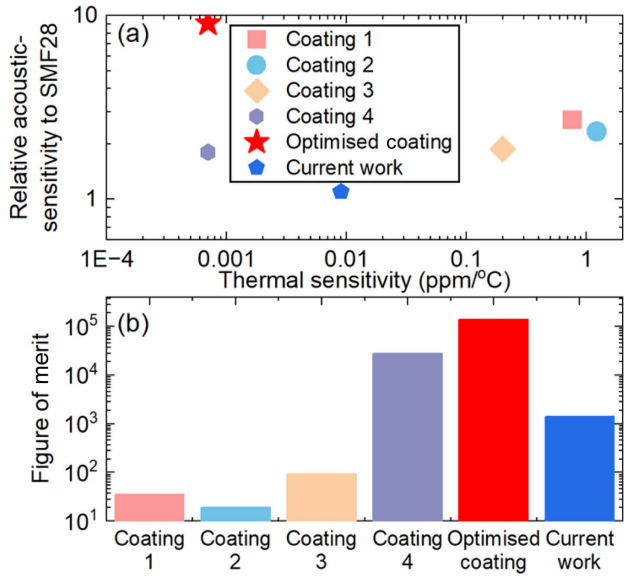

Fig. 13. Calculated acoustic/thermal response of ULE-HCF with the same air hole size ($a = 45$ μm) and cladding radius ($b = 62.5$ μm) as well as different coating materials. Coating 1: 30 μm acrylate (Young's modulus: 200 MPa; Poisson's ratio: 0.37; and CTE: 110 ppm/°C); Coating 2: 20 μm fluorinated acrylate (Young's modulus: 800 MPa; Poisson's ratio: 0.37; and CTE: 70 ppm/°C); Coating 3: 5 μm polyimide (Young's modulus: 4800 MPa; Poisson's ratio: 0.34; and CTE: 10 ppm/°C); Coating 4: 90 μm silicone (Young's modulus: 1 MPa; Poisson's ratio: 0.499; and CTE: 200 ppm/°C); optimized coating: same properties as silicone, but with a Poisson's ratio of 0.3. The four coating materials are chosen based on literature [27].

level of acoustic sensitivity. This increased acoustic sensitivity is mainly due to ULE glasses with reduced Young's modulus of 67.6 GPa compared to silica modulus of 72 GPa. This leads to a significant improvement in performance, confirmed by FoM > 1000.

B. Further Optimization of Acoustic/Thermal ULE-HCF Response

Although ULE-HCFs exhibit exceptionally low thermal sensitivity due to the ultra-low expansion coefficient of the ULE glass, their acoustic sensitivity in the current configuration is not fully optimized. Based on the theoretical analysis introduced in Section 2, we have further investigated how different coating materials will affect the acoustic and thermal performance of ULE-HCFs.

Figure 13(a) compares the relative acoustic sensitivity in respect to SMF28 and thermal sensitivity of ULE-HCFs with four coating materials that have been used on optical fibers, all modeled with a fixed air hole radius $a = 45$ μm and a cladding radius $b = 62.5$ μm. The ULE's CTE is considered as −0.04 ppm/°C [29]. The coating thickness is set based on practical constraints related to fiber protection and its contribution to acoustic sensitivity enhancement. The corresponding FoMs, plotted in Fig. 13(b), span more than four orders of magnitude across the considered coating materials. Among them, silicone yields the highest FoM, primarily due to its minimal impact on thermal sensitivity. However, its near-incompressible nature (Poisson's ratio ∼0.5) limits the extent of acoustic enhancement it can offer. We demonstrate this by considering a fifth coating material, which would have the same properties as silicone but a smaller Poisson's ratio of 0.3. Our current configuration is marked by a blue pentagon, which shows clear room for performance enhancement in both acoustic sensitivity and FoM when implementing silicone coating (violet hexagon, Coating 4). Further improvements could be expected if a coating with small Young's modulus could be complemented with small Poisson's ratio (red star).

6. CONCLUSION

In this work, we have presented a comparative study on the acoustic and thermal response of hollow-core fibers (HCFs). We first developed a model to simulate the acoustic sensitivity of HCFs. By varying cladding diameter, air hole size, coating thickness, and mechanical parameters, such as coating's Young's modulus and Poisson's ratio, we examined their respective influences on acoustic sensitivity and temperature cross-sensitivity. A figure of merit (FoM) was introduced to evaluate the trade-off between acoustic response and thermal stability and show that silica-made HCFs can reduce temperature cross-sensitivity as compared to single-mode fiber (SMF28e).

The theoretical analysis is then validated with four different HCFs, three made from silica and one made from ULE glass. While improvement in FoM for silica-made HCFs as compared to SMF is significant (by a factor of 14 to 28 in our experiments, depending on the HCF design), large further improvement is achieved in the ULE-HCF with FoM improvement >1000. ULE-HCF exhibits an acoustic response at a similar level to SMF28e, while offering extremely low thermal sensitivity (>1000 times better than SMF28e), a feature attributed to the near-zero coefficient of thermal expansion of the ULE glass. Our analysis also shows that by carefully selecting the dimensions of the HCFs and the coating material, ULE-HCF's acoustic sensitivity could be further improved by an order of magnitude with simultaneous reduction in the thermal

sensitivity by an order of magnitude, leading to two orders of magnitude FoM improvement.

These findings pave the way for the next generation of fiber-based acoustic sensors that combine strong low-frequency response with exceptional thermal stability, meeting the challenge of temperature crosstalk in low-frequency acoustic sensing. Besides, the FoM introduced in this work reflects intrinsic acoustic and thermal properties of the fiber and is therefore independent of the specific acoustic field distribution. Therefore, this could be combined with distributed measurement, something routinely implemented in SMF-based systems, given early reports indicating its feasibility in HCFs [37]. It can also extend to long-baseline monitoring of geophysical activity, civil infrastructure, and equipment-health in harsh, thermally dynamic environments.

Funding. Engineering and Physical Sciences Research Council (EP/W037440/1).

Disclosures. The authors declare no conflicts of interest.

Data Availability. The data underpinning the research presented are accessible through the University of Southampton research repository [38].

REFERENCES

1. G. Marra, C. Clivati, R. Luckett, *et al.*, "Ultrastable laser interferometry for earthquake detection with terrestrial and submarine cables," Science **361**, 486–490 (2018).
2. H. Xiao, Z. J. Spica, J. Li, *et al.*, "Detection of earthquake infragravity and tsunami waves with underwater distributed acoustic sensing," Geophys. Res. Lett. **51**, e2023GL106767 (2024).
3. P. Jousset, G. Currenti, B. Schwarz, *et al.*, "Fibre optic distributed acoustic sensing of volcanic events," Nat. Commun. **13**, 1753 (2022).
4. F. Muñoz, J. Urricelqui, M. A. Soto, *et al.*, "Finding well-coupled optical fiber locations for railway monitoring using distributed acoustic sensing," Sensors **23**, 6599 (2023).
5. E. Sidenko, K. Tertyshnikov, M. Lebedev, *et al.*, "Experimental study of temperature change effect on distributed acoustic sensing continuous measurements," Geophysics **87**, D111–D122 (2022).
6. O. C. Akkaya, O. Kilic, M. J. F. Digonnet, *et al.*, "High-sensitivity thermally stable acoustic fiber sensor," in *IEEE Sensors* (IEEE, 2010), pp. 1148–1151.
7. S. Tanaka, H. Yokosuka, and N. Takahashi, "Temperature-independent fiber Bragg grating underwater acoustic sensor array using incoherent light," Acoust. Sci. Technol. **27**, 50–52 (2006).
8. O. C. Akkaya, O. Akkaya, M. J. F. Digonnet, *et al.*, "Modeling and demonstration of thermally stable high-sensitivity reproducible acoustic sensors," J. Microelectromech. Syst. **21**, 1347–1356 (2012).
9. N. Bradley, K. E. Haavik, and M. Landrø, "Estimation of temperature profiles using low-frequency distributed acoustic sensing from in-well measurements," SPE J. **29**, 314–327 (2024).
10. J. Li, H. Liu, Y. Xiao, *et al.*, "High-sensitivity simultaneously distributed acoustic and temperature sensing by an air-ring microstructured optical fiber," Opt. Lett. **50**, 3608–3611 (2025).
11. J. D. Pelaez Quiñones, A. Sladen, A. Ponte, *et al.*, "High resolution seafloor thermometry for internal wave and upwelling monitoring using distributed acoustic sensing," Sci. Rep. **13**, 17459 (2023).
12. B. Liu, R. Liang, H. Deng, *et al.*, "Demodulation of EFPI-FBG hybrid optical microphone based on spectrum analysis," IEEE Sens. J. **22**, 8499–8508 (2022).
13. F.-X. Launay, M. Doisy, R. Larda, *et al.*, "All-optical hydrophone insensitive to temperature and to static pressure," U.S. patent 9,103,713 (11 August, 2015).
14. W. Wang, "Fabry-Perot interference fiber acoustic wave sensor based on laser welding all-silica glass," Materials **15**, 2484 (2022).
15. M. Ding, M. Komanec, D. Suslov, *et al.*, "Long-length and thermally stable high-finesse Fabry-Perot interferometers made of hollow core optical fiber," J. Lightwave Technol. **38**, 2423–2427 (2020).
16. S. N. Turtaev, M. I. Belovolov, A. E. Levchenko, *et al.*, "Acoustic sensitivity of the negative curvature hollow core fiber," in *International Conference Laser Optics* (IEEE, 2014), p. 1.
17. M. Pang and W. Jin, "Detection of acoustic pressure with hollow-core photonic bandgap fiber," Opt. Express **17**, 11088–11097 (2009).
18. F. Yang, W. Jin, H. L. Ho, *et al.*, "Enhancement of acoustic sensitivity of hollow-core photonic bandgap fibers," Opt. Express **21**, 15514–15521 (2013).
19. L. Jin, B.-O. Guan, and H. Wei, "Sensitivity characteristics of Fabry-Perot pressure sensors based on hollow-core microstructured fibers," J. Lightwave Technol. **31**, 2526–2532 (2013).
20. M. Petrovich, E. N. Fokoua, Y. Chen, *et al.*, "Broadband optical fibre with an attenuation lower than 0.1 decibel per kilometre," Nat. Photonics **19**, 1203–1208 (2025).
21. Y. Chen, M. N. Petrovich, E. N. Fokoua, *et al.*, "Hollow core DNANF optical fiber with <0.11 dB/km loss," in *Optical Fiber Communication Conference (OFC)* (Optica Publishing Group, 2024), paper Th4A.8.
22. E. N. Fokoua, S. A. Mousavi, G. T. Jasion, *et al.*, "Loss in hollow-core optical fibers: mechanisms, scaling rules, and limits," Adv. Opt. Photonics **15**, 1–85 (2023).
23. R. Slavík, E. R. N. Fokoua, M. Bukshtab, *et al.*, "Demonstration of opposing thermal sensitivities in hollow-core fibers with open and sealed ends," Opt. Lett. **44**, 4367–4370 (2019).
24. Z. Zhao, M. MacAlpine, and M. S. Demokan, "The directionality of an optical fiber high-frequency acoustic sensor for partial discharge detection and location," J. Lightwave Technol. **18**, 795–806 (2000).
25. S. P. Timoshenko and J. N. Goodier, *Theory of Elasticity*, 3rd ed. (McGraw-Hill, 1970).
26. W. Zhu, E. R. N. Fokoua, A. A. Taranta, *et al.*, "The thermal phase sensitivity of both coated and uncoated standard and hollow core fibers down to cryogenic temperatures," J. Lightwave Technol. **38**, 2477–2484 (2020).
27. R. Janani, D. Majumder, A. Scrimshire, *et al.*, "From acrylates to silicones: a review of common optical fibre coatings used for normal to harsh environments," Prog. Org. Coatings **180**, 107557 (2023).
28. B. Shi, H. Sakr, J. Hayes, *et al.*, "Thinly coated hollow core fiber for improved thermal phase-stability performance," Opt. Lett. **46**, 5177–5180 (2021).
29. M. Ding, I. A. Davidson, G. Jasion, *et al.*, "Hollow-core fiber made of ultralow expansion glass: toward the ultimate stability for room-temperature fiber optics," Sci. Adv. **11**, eads7529 (2025).
30. S. Gao, H. Chen, Y. Sun, *et al.*, "Fourfold truncated double-nested antiresonant hollow-core fiber with ultralow loss and ultrahigh mode purity," Optica **12**, 56–61 (2025).
31. G. A. Mahdiraji, J. Rzegocki, I. A. Davidson, *et al.*, "Bend insensitive hollow core DNANF with SMF-matching mode field diameter and 125 μm outer diameter for low loss direct interconnection in short reach applications," in *Optical Fiber Communication Conference (OFC)* (Optica Publishing Group, 2024), paper M3J.5.
32. J. H. Osório, F. Amrani, F. Delahaye, *et al.*, "Hollow-core fibers with reduced surface roughness and ultralow loss in the short-wavelength range," Nat. Commun. **14**, 1146 (2023).
33. I. A. Davidson, G. Jackson, N. K. Baddela, *et al.*, "Thinly coated hollow-core fibers: how thin can we go?" Proc. SPIE **13522**, 1352209 (2025).
34. L. Wu, P. R. White, and P. Kemp, "Measurements of the resonance properties of dummy fish swim bladders," in *Advances in Hydraulic Research* (Springer, 2024), pp. 397–407.
35. B. Shi, C. Zhang, T. Kelly, *et al.*, "Splicing hollow-core fiber with standard glass-core fiber with ultralow back-reflection and low coupling loss," ACS Photonics **11**, 3288–3295 (2024).
36. B. Shi, I. A. Davidson, G. A. Mahdiraji, *et al.*, "Optimizing hollow core fibers for stable interferometry," in *Joint Conference of the European*

Frequency and Time Forum and IEEE International Frequency Control Symposium (EFTF/IFCS) (IEEE, 2023), pp. 1–2.

37. N. K. Fontaine, M. Mazur, B. J. Puttnam, *et al.*, "Ultra-high resolution and long-range OFDRs for characterizing and monitoring Hollow-core DNANFs," in *Optical Fiber Communication Conference (OFC)* (Optica Publishing Group, 2025), paper Th4D.6.
38. N. Ding, W. Wu, K. William, *et al.*, "Dataset for towards low-frequency acoustic sensing using antiresonant hollow-core fibers," SOTON, https://eprints.soton.ac.uk/508529/ (2026).